RESEARCH ARTICLE

An Evaluation Model of Star Sensor Observation Capability Under Hypersonic Aerothermal Conditions

BING CHEN[1], YONG ZHENG[1], BIN XU[1], CHONGHUI LI[1], AND FENGNA GE[2]
[1]Information Engineering University, Zhengzhou, Henan 450001, China
[2]Business School, Henan University, Kaifeng, Henan 475004, China

Corresponding author: Fengna Ge (gena2002@163.com)

ABSTRACT During hypersonic flight in the atmosphere, severe aerothermal effects occur on the optical hood or observation window of an aircraft, keeping the optical window and surface flow field in a high-temperature state, as well as causing a large amount of radiation and strong background noise. These phenomena have serious effects on the observation capability of star sensors. An evaluation model of star sensor observation capability under hypersonic aerothermal conditions was constructed in this study, using a definition of the signal-to-noise ratio considering defocused intense radiation sources. Furthermore, a method of calculating the observable limiting magnitude under aerothermal conditions is given. The model was used in simulation tests involving different flight states and temperature conditions. The results showed that the thermal radiation of the aircraft observation window has the greatest influence, which is more than two orders higher than that of the outer flow near the window; when the window temperature was controlled below 750 K, for a star sensor with an SNR threshold of 3, navigation stars with magnitudes brighter than 5 could be captured in the visible band of 0.35–0.7 μm, and the near-infrared band of 0.9–1.4 μm was unavailable.

INDEX TERMS Hypersonic aerothermal condition, star sensor, observation capability, evaluation, SNR, limiting magnitude.

I. INTRODUCTION

Hypersonic vehicles, which are aircrafts with maximum flight speed greater than Mach 5, are crucial for future strategic stability with their superior maneuverability and penetration ability [1]. Hypersonic flights are heavily dependent on navigation and guidance information such as position, velocity, and attitude [2]. In the context of high-intensity navigation confrontation, hypersonic vehicles must have reliable autonomous navigation ability; that is, they must be able to rely on their own equipment, obtain relevant information independently, and carry out navigation tasks without exchanging information with the outside world [3]. Astronomical navigation technology can improve the reliability of autonomous navigation for hypersonic vehicles by using

stars for navigation; this approach provides high-precision orientation information, performs key course and attitude corrections, and can effectively mitigate the error divergence of inertial navigation systems. This technology has been widely used in the fields of aeronautics and astronautics [4].

The foundations of astronomical navigation are the star map capture and identification processes performed by star sensors. Hypersonic flights cause aerodynamic effects in the vicinity of the star sensor's observation window, degrading the star map and star identification performance [5], and thus decreasing the feasibility of astronomical navigation. Several previous studies have attempted to address the beam correction problem. Chen et al. proposed a shock deflection correction method based on an analytical solution to reduce the beam deflection caused by the shock wave and mixed layer on the surface of the observation window in hypersonic flight [6]. Sudarshanam et al. presented a correction method

The associate editor coordinating the review of this manuscript and approving it for publication was Fabrizio Santi.

based on optical phase conjugation [7], and Rennie et al. developed a simple yet effective feedforward adaptive-optic correction strategy for optical aberrations [8]. Guo and Luo provided an adaptive-optic method of correcting aero-optical wavefront distortions based on flow control [9]. However, all of these methods are based on the same basic assumption that the target signal is significantly stronger than the background radiation, which is hard to obtain in hypersonic astronomical observations.

Far-field radiation, such as atmospheric background radiation, is treated as an important factor affecting star map capture and identification. Multi-field-of-view technology, short-wave infrared band sensors, and optimized star catalogs have been used to improve navigation starlight capture under far-field brightness [10], [11]. Ding et al. believed that the image quality could be improved and the difficulty of wavefront adaptive correction could be reduced by appropriately extending the exposure time [12].

The background radiation near the optical aperture must be considered in astronomical observations performed by hypersonic vehicles. When the observation window is kept exposed in a hypersonic flight environment, continuous hypersonic aerodynamic heating leads to heat flux from the window and flow field nearby, forming strong radiated background noise on the star map [13]. As a result, the ability of the star sensor to capture stars is reduced, and star point information cannot be collected in the field of view of the sensor, affecting the attitude accuracy [14]. According to Ni et al., this problem can be mitigated by a tightly coupled integrated navigation approach [15]. Zhang et al proposed that the thermal adaptability of photoelectric sensors could be improved by optimizing their structural design [16]. Chen et al. [17] and Zhao et al. [18] conducted prototype operation tests and wind tunnel tests but did not sufficiently assess the steady background radiation due to aerothermal conditions. It is necessary to evaluate the observation capability of star sensors under intense radiation near the optical aperture; this could provide quantitative guidance for improving the external environment of the observation window and optimizing sensor performance.

In this paper, a framework for evaluating the observation ability of a star sensor under hypersonic aerodynamic heating conditions is proposed in Section II, which also includes a definition of the signal-to-noise ratio (SNR) considering defocused intense radiation sources. Imaging models of far- and near-field radiation sources are analyzed in Section III. A calculation model for the limiting magnitude of stars that surpass the required SNR threshold without saturation is described in Section IV. Section V provides the relationship between the limiting magnitude of observable stars and the window temperature, based on simulation tests and analyses using different flight states and temperatures.

II. MODELING APPROACH
Navigation stars were treated as uniform point light sources at a distance of infinity. Therefore, the star sensor can capture and analyze the navigation star without noting the detection distance, morphology structure, or radiation distribution of the star itself [19]. The observation capability of a star sensor is different from the number of detected stars, which depends on the field of view, altitude, and galactic latitude. The observation capability evaluation of star sensors under hypersonic aerothermal conditions focuses on the comparison of star signals and radiated noise from the far and near fields, as well as the influence of these conditions on star map acquisition and recognition. Imaging saturation was investigated, that is, whether the self-radiation of the high-temperature optical window and flow field can cause overexposure of the star map. Image deterioration was also considered, that is, whether the SNR of the star point can be controlled within the discernible range after hypersonic aerothermal heating.

A. FRAMEWORK OF EVALUATION
The continuous convective heating of hypersonic incoming flow causes a local hyperthermal environment around the observation window. If the signal received by the star sensor causes pixel well saturation, the star map will be overexposed and the star point information will be lost. If the SNR is too low, the information of the navigation star will be drowned out by the noise, and making star identification difficult. If the limiting magnitude of stars is too bright, the number of observable stars will be reduced and the reliability of attitude determination during the flight will be compromised. Therefore, the standard for evaluating the observation capability of a hypersonic star sensor can be expressed by the limiting magnitude of stars that surpass the required SNR threshold without saturation.

The evaluation framework of hypersonic astronomical observation capability is shown in Fig. 1. The input of the framework includes four kinds of parameters: environmental, hypersonic operation, telescope, and star sensor parameters. Environmental and hypersonic operations parameters directly influence aerothermal effects, as well as the flux from different radiation sources. Telescope structure parameters determine the imaging performance of the radiation source. Finally, the sensor parameters restrict the bottom noise and the final imaging results. For radiation sources far from the optical aperture, such as navigation stars and atmospheric radiation, an imaging model of far-field radiation sources, as described in Section III.A, can be used. For the thermal radiation of the optical window and the nearby flow, it is necessary to use the imaging model of defocused radiation sources as described in Section III.B, for radiation calculation.

B. DEFINITION OF SNR CONSIDERING DEFOCUSED RADIATION SOURCE
SNR is one of the most important indicators for sensors. An observation system can effectively detect the target only when it reaches a certain SNR [20]. The common method of calculating SNR is the accurate and convenient electronic number method, which converts the target and noise signals into electrons through quantum efficiency (QE) [21]. The common definition of SNR refers to the ratio of the target signal to the noise generated by the focal plane due to the
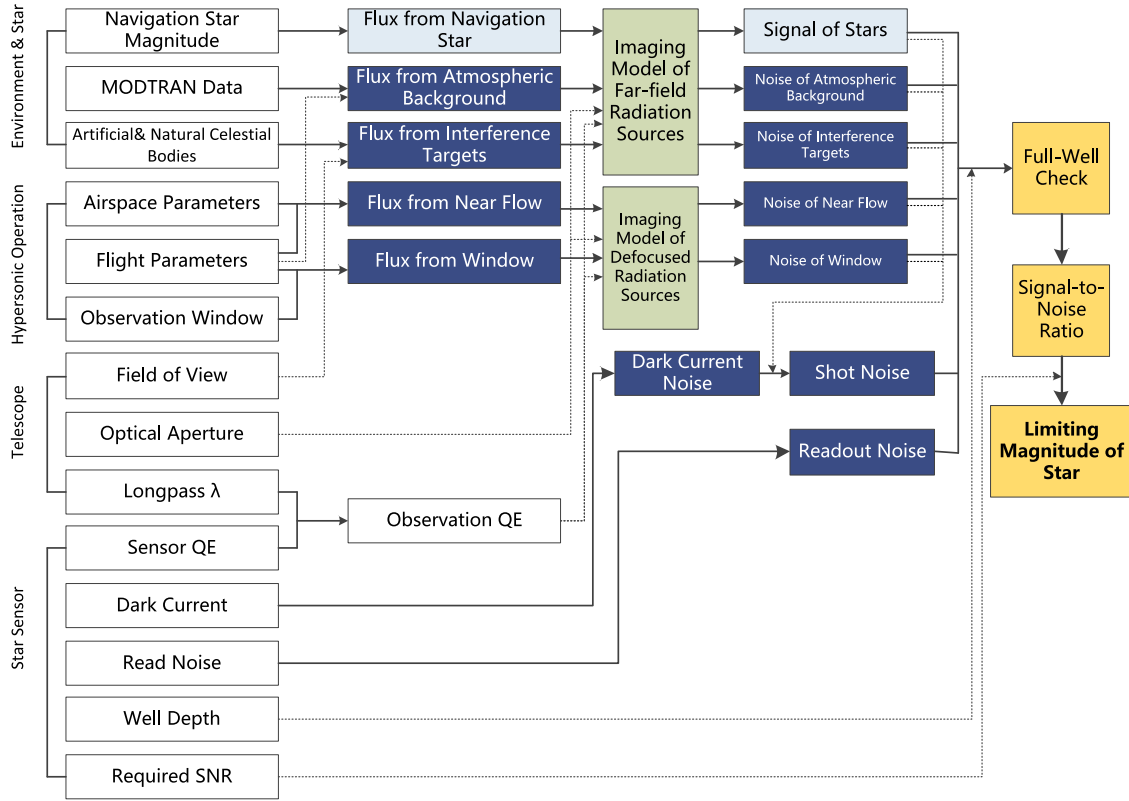
FIGURE 1. Evaluation framework of observation capability under hypersonic thermal conditions.

reception of photons. The formula for SNR can be given as follows [22]:

$$\text{SNR}_t = \frac{\mu_m}{n_{fp}}$$

$$= \frac{\mu_m}{\sqrt{\mu_m + \mu_{atmos} + \mu_{flow} + \mu_{window} + \mu_{dark} + \sigma_{read}^2}}$$

(1)

In (1), μ_m represents the number of electrons generated by the navigation stars of magnitude m, n_{fp} is the total number of electrons induced by the shot noise and readout noise, μ_{atmos} is the number of electrons generated by the atmospheric background, and μ_{flow} is the number of electrons generated by the thermal flow near the observation window. μ_{window} is the number of electrons generated by observation window radiation, μ_{dark} is the number of electrons generated by the dark current, and σ_{read} is the standard deviation of the number of electrons generated by readout noise [23]. It is generally believed that the noise generated by the sensor itself is evenly distributed across all pixels of the entire photosensitive component.

The intense aerothermal effect caused by hypersonic flight makes the radiation noise near the optical aperture non-negligible. This radiation noise is located in the defocusing range, which also makes the method of evaluating the observation capability of star sensors on hypersonic vehicles different from that for sensors on conventional spacecraft.

Under the condition of hypersonic aerodynamic heating, the noise caused by the navigation star signal, focal plane being irradiated, and noise effects of defocused and far-field radiation sources should be taken into account. The definition of SNR considering the noise of defocused radiation sources can be written as follows:

$$\text{SNR} = \frac{\mu_m}{\mu_{atmos} + \mu_{flow} + \mu_{window} + n_{fp}}$$

(2)

n_{fp} has the same expression as in (1).

C. FULL-WELL INSPECTION

For observation systems based on the photoelectric effect, if the number of electrons on the pixel exceeds a certain number, the pixel potential well will appear as a "full well," resulting in overexposure of the image. It will then be impossible to extract comparative information at the pixel level. Therefore, the "full well" at the pixels of the focal plane should be used as an important index to evaluate astronomical observation performance. The calculation index $f(m)$ for judging whether a star of magnitude m causes a pixel "full-well" is given as follows:

$$f(m) = \mu_m + \mu_{atmos} + \mu_{flow} + \mu_{window} + n_{fp} - N_{pixel}$$

(3)

In (3), N_{pixel} represents the number of "full-well" electrons at a pixel. $f(m) \geq 0$ means that the signal and noise at the pixel have been saturated. The amount of information

captured in the star map will decrease significantly if a large range of continuous pixels on the focal plane is full-well.

The full-well capacity of photosensitive components used in imaging chips has been increasing in recent years. The common full-well capacity of a complementary metal-oxide-semiconductor (CMOS) sensor in the visible band can reach to $10^5 e^-$. Some shortwave infrared imaging chips have a single pixel full-well capacity of $8 \times 10^5 e^-$ [24].

III. IMAGING MODELS OF RADIATION SOURCES

A. IMAGING MODEL OF FAR-FIELD RADIATION SOURCES

Magnitude is used to describe the ability of objects to emit light in astronomical observations. The results observed on Earth are expressed as apparent magnitudes. If m_1 and m_2 are used to represent the apparent magnitudes of two stars, then the irradiance of those two stars E_1 and E_2 satisfies (4):

$$\frac{E_2}{E_1} = 2.512^{m_1 - m_2} \tag{4}$$

The sun can be regarded as a radiation black body with a temperature of 5900 K. By Planck's law, the sun's exitance in the band 0.45–0.9 μm can be obtained as follows:

$$M_{solar} = \int_{0.45}^{0.9} \frac{c_1 \lambda^{-5}}{\exp\left[c_2/(\lambda T)\right] - 1} d\lambda \tag{5}$$

In (5), c_1 and c_2 are the first and second radiation constant in Planck's law, respectively. The irradiance E_{solar} of the sun in this band at the outer surface of Earth's atmosphere satisfies (6).

$$E_{solar} = M_{solar} \frac{S_{solar}}{4\pi (r_{se})^2} \tag{6}$$

In (6), S_{solar} is the surface area of the solar photosphere and r_{se} is the average distance between the sun and Earth.

The apparent magnitude of the sun is known as -26.74. Based on the sun-to-Earth irradiance E_{solar}, E_m, the irradiance of the navigation star of magnitude m to Earth can be given as (7), with the calculated irradiance of the sun to Earth by (6).

$$E_m = E_{solar} \times 2.512^{-26.74 - m} \tag{7}$$

In (7), it was assumed, for simplicity, that the stars have the same spectral distribution as the sun. Within the exposure time t, the number of electrons produced by the projection of starlight radiation onto the photosensitive component can be marked as μ_m, which can be written as follows:

$$\mu_m = \int_{\lambda_1}^{\lambda_2} E_m(\lambda, T) \cdot \tau_{atmos}(H, \theta, \lambda) \cdot \tau_{flow}(\lambda)$$
$$\cdot \tau_{window}(\lambda) \cdot \tau_{opt}(\lambda) \cdot t \cdot S_{opt} \cdot QE(\lambda)/W_{ph} d\lambda \tag{8}$$

In (8), $E_m(\lambda, T)$ represents the irradiance of a star of magnitude m and temperature T to the Earth in the λ band, in $W \cdot m^{-2}$ units. $\tau_{atmos}(H, \theta, \lambda)$ is the atmospheric transmittance at observation height H and zenith angle θ. $\tau_{window}(\lambda)$ and $\tau_{opt}(\lambda)$ represent the spectral transmittance of the observation window and optics at wavelength λ, respectively. S_{opt}

is the area of the aperture of the optical system; λ_1, λ_2 represent the operating band of the detector, $W_{ph} = hc/\lambda$ is the energy carried by a single photon, and $QE(\lambda)$ is the quantum efficiency of the photosensitive component, h is the Planck's constant and c is the speed of light in vacuum.

Similarly, atmospheric background radiation can be treated as far-field radiation. During the exposure time t, the number of electrons μ_{atmos} produced by the atmospheric background radiation projected onto the sensor can be given as follows:

$$\mu_{atmos} = \int_{\lambda_1}^{\lambda_2} L_{\lambda, atmos} \cdot \tau_{atmos}(\lambda) \cdot \tau_{flow}(\lambda) \cdot \tau_{window}(\lambda)$$
$$\cdot \tau_{opt}(\lambda) \cdot t \cdot S_{opt} \cdot QE(\lambda) \cdot \Omega / W_{ph} d\lambda \tag{9}$$

In (9), $L_{\lambda, atmos}$ is the atmospheric background radiation intensity under a given observation condition, in units of $W \cdot m^{-2} \cdot \mu m^{-1} \cdot sr^{-1}$, and Ω represents solid angle corresponding to the photosensitive component, in units of sr.

B. IMAGING MODEL OF DEFOCUSED RADIATION SOURCES

The observation window and the flow nearby are kept in a high-temperature state during hypersonic flight, which forms defocused radiation sources that affect the star sensor. This phenomenon will be discussed for a case in which the focal length is less than the object distance of the telescope system ($f < l$). The radiation micro-facet located at the defocus argument should be imaged at the theoretical image point (TIP), but owing to the occlusion of the focal plane, the energy is distributed within the circular area on the focal plane, as shown in Fig. 2. This circle can be called the "illuminated circle," with diameter denoted as R.
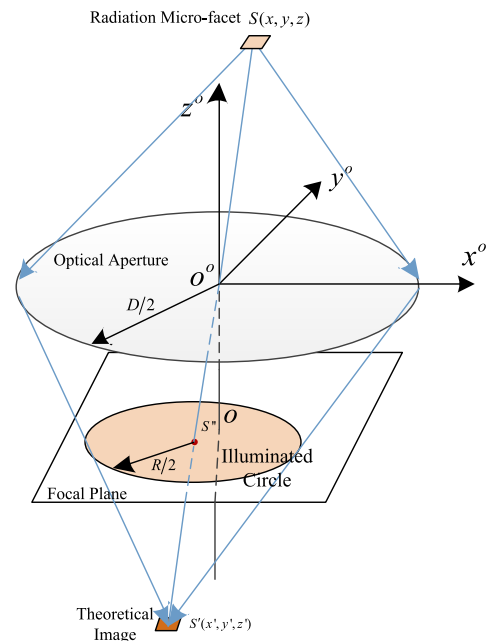

FIGURE 2. Diagram of focal plane illuminated in $f < l$.

According to the similarity of the geometric relations between the illuminated circle and the diameter of the optical aperture D, we obtain:

$$\frac{D}{R} = \frac{l'}{l' - f} \tag{10}$$

Combined with the conditions $l' = fl/(l - f)$, we obtain:

$$R = \frac{f}{l}D \tag{11}$$

When the optical system focal length is greater than the object distance ($l < f$), the radiation micro-facet cannot be imaged on the other side of the optical aperture, but the energy is equivalent to the effect of radiation from the virtual image point through the optical aperture. The irradiated area is often much larger than the focal plane, which makes the energy highly dispersed. With geometric relations, the diameter of the illuminated circle R can be written as follows:

$$R = \frac{f + l'}{l'}D = \frac{f}{l}D \tag{12}$$

In summary, a part of the energy from the radiation micro-facet can illuminate the focus plane; this mainly depends on the position of the radiation micro-facet, as well as the parameters of the telescope system.

According to the reversible rule of optical paths, the TIP dS' formed by the radiation micro-facet through the optical system can be marked as the new radiation source. The exitance of TIP dS' is denoted as $M_{dS'}$, which can be calculated using the irradiance $E_{dS'}$ from the radiant flux ϕ through the optical aperture as follows:

$$M_{dS'} = E_{dS'} = \tau_o \frac{\phi}{dS'}$$
$$\phi = \int_S \int_{\pi(D/2)^2} L d\Omega dS \tag{13}$$

In (13), ϕ represents the radiation flux emitted by the radiation micro-facet dS to the optical aperture of area $\pi(D/2)^2$. The transmittance of the optical system is marked as τ_o.

The TIP dS' is a micro-facet emitted in a specific direction with uniform radiance $L_{dS'}$. The relationship between $L_{dS'}$ and $M_{dS'}$ can be calculated as follows:

$$L_{dS'} = \frac{M_{dS'}}{\Omega_{ic}} \tag{14}$$

Ω_{ic} is the solid angle from TIP dSn' to the full illuminated circle. The irradiated region on the focal plane is denoted as S_{pixel}, which can be obtained by using the relations shown in Fig. 2. The solid angle from TIP dS' to the irradiated region is denoted as Ω_{pixel}. The radiation flux ϕ_{pixel} on the area S_{pixel} from TIP can be written as follows:

$$\phi_{pixel} = \int_{S'} L_{dS'} \Omega_{pixel} dS' \tag{15}$$

In (15), S' represents the total area of theoretical imaging of the entire radiation source. The product of radiation flux ϕ_{pixel} and exposure time is the amount of radiation source energy captured in the pixel.

IV. LIMITING MAGNITUDE CALCULATION WITH AN SNR THRESHOLD

If the required SNR threshold of the star sensor is set as SNR_0, the following can be obtained from (2):

$$\frac{\mu_m}{\mu_{atmos} + \mu_{flow} + \mu_{window} + n_{fp}} \geq SNR_0 \tag{16}$$

Equation (16) can be transformed as follows:

$$(\mu_m - AC)^2 \geq C^2 \mu_m + C^2(A + B) \tag{17}$$

In (4), the parameters A, B, and C can be expressed as follows:

$$A = \mu_{atmos} + \mu_{flow} + \mu_{window}$$
$$B = \mu_{dark} + \sigma_{read}^2$$
$$C = SNR_0$$

The one unknown μ_m in the above equation can be solved analytically as follows:

$$\mu_m \geq \left(AC + \frac{C^2}{2}\right) + \sqrt{\left(AC + \frac{C^2}{2}\right)^2 - C^2\left(A^2 - A - B\right)} \tag{18}$$

By using (7), we obtain:

$$\mu_m = k \times 2.512^{-26.74-m} \times E_{solar} \tag{19}$$

In (19), k is the proportion of energy occupied by a single pixel in the illuminated circle.

$$k \times 2.512^{-26.74-m} \times E_{solar} \geq \left(AC + \frac{C^2}{2}\right)$$
$$+ \sqrt{\left(AC + \frac{C^2}{2}\right)^2 - C^2\left(A^2 - A - B\right)} \tag{20}$$

The limiting magnitude m can then be solved as follows:

$$m \leq -\log_{2.512}\left\{\left[\sqrt{\left(AC + \frac{C^2}{2}\right)^2 - C^2\left(A^2 - A - B\right)}\right.\right.$$
$$\left.\left. + \left(AC + \frac{C^2}{2}\right)\right] \cdot \frac{1}{k} \cdot \frac{1}{E_{solar}}\right\} - 26.74 \tag{21}$$

V. SIMULATION AND ANALYSIS
A. SIMULATION CONDITION

The flight altitude was set as 20 km. The flight speed was set as Mach 5, and the ambient temperature was 216.65 K. Atmospheric transmittance $\tau_{atmos}(\lambda)$ was set as 0.99.

The diameter of the optical aperture D was set as 50 mm. The distance from the inner surface of the observation window to the optical aperture, l_{window}, was set as 100 mm. Research has shown that when the thickness of the observation window is about 15 mm, the intensity and detection sensitivity of the window reach a relative equilibrium [25], [26]. Thus, the distance from the equivalent blackbody facets
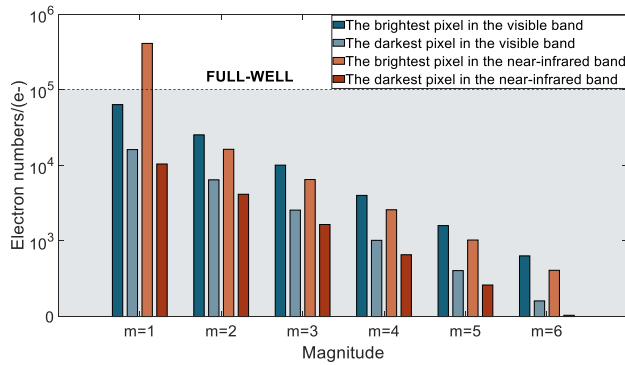
FIGURE 3. Electronic numbers generated in the brightest and darkest pixels by stars of magnitude 1–6.

TABLE 1. The average electronic numbers on pixels generated by hyperthermal window and outer flow. (unit: e^-).

Waveband (μm)	Temperature (K)	Average electron number	
		Window	Outer flow
0.35–0.7	1300	5.0225×10^5	0.7416
	900	2.9688×10^2	3.7749×10^{-5}
	750	2.5319	1.1947×10^{-7}
	600	2.1×10^{-3}	4.8261×10^{-11}
0.9–1.4	1300	2.5014×10^8	9.3585×10^5
	900	4.8938×10^6	5.5793×10^2
	750	4.0488×10^5	28.9092
	600	1.0244×10^4	0.5288

of the outer flow to the optical aperture surface, l_{fluid}, was set as 115 mm. The dark current of the sensor was set as 19000 e^-/s, while the read noise $\sigma^2_{read} = 80e^-$. The star sensor exposure time was 0.1 seconds. Finally, the full-well capacity of a single pixel was set as $10^5 e^-$.

Parameters such as the quantum efficiency QE(λ) and optical aperture transmittance $\tau_{opt}(\lambda)$ were simplified in the simulations, and their correlation to the spectral band is ignored. Thus, these parameters were assumed to be constants. The emissivity $\varepsilon_{window}(\lambda)$ and transmittance $\tau_{window}(\lambda)$ of the hyperthermal window were set as 0.8 and 0.9 respectively. For signals of 0.35–0.55 μm and above 0.7 μm, QE was set as 0.1. For signals of 0.55–0.7 μm, QE was set as 0.15. The brightness value of the sky was set as $4 \times 10^3 cd/m^2$. The effect of the azimuth on atmospheric background radiation and flux from interference targets was ignored in simulation tests.

B. RESULTS OF THE SIMULATIONS

1) ELECTRONS PRODUCED BY NAVIGATION STARS OF DIFFERENT MAGNITUDES

The energy from a navigation star is distributed over 3×3 pixels on the focal plane. One pixel with the highest energy accounted for 22.3%, each of the four medium-energy pixels accounted for 11.2%, and each of the last four pixels had 5.67% of the total energy [27]. Thus, the electronic distribution generated by the star of magnitude m was obtained.

In the visible light band of 0.35–0.7 μm and the near-infrared light band of 0.9–1.4 μm, the distribution of electronic numbers generated by stars of magnitude 1–6 is shown in Fig.3. Only stars of magnitude 1 cause the brightest pixel to be full-well.

2) ELECTRONS PRODUCED BY DEFOCUSED RADIATION SOURCES

According to the calculation model of focal plane radiation by defocused radiation elements given in Section II, the radiant emittance of the observation window and outer flow at high temperature can be determined. The irradiation of the defocused radiation sources on the focal plane is obtained using

the equivalent blackbody facets calculation method [28], then finally converted into the number of electrons on each pixel.

The average electronic numbers for pixels generated by the hyperthermal window and outer flow in the visible and near-infrared bands are presented in Table 1.

It is obvious that the electronic numbers from the hyperthermal window are much greater than those from the outer flow. In the visible band, the number of electrons generated by hyperthermal window is nearly six orders of magnitudes higher, while the gap drops to three orders of magnitudes in the near-infrared band.

In the bands of 0.35–0.7 μm and 0.9–1.4 μm, under different temperature conditions, the maximum and minimum numbers of electrons generated for pixels by the hyperthermal window are shown in Fig.4.
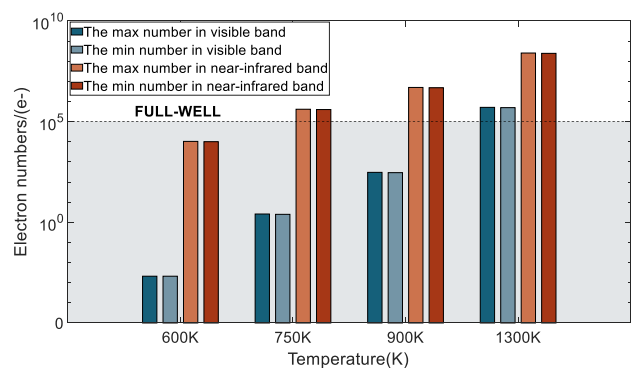

FIGURE 4. The maximum and minimum electronic numbers produced by the hyperthermal window in the pixels.

In the same two bands, under different temperature conditions, the maximum and minimum numbers of electrons generated for pixels by the outer flow at high temperature is shown in Fig.5.

There is little difference between the maximum and minimum electron numbers caused by the same defocused radiation source. That means the defocused radiation of the

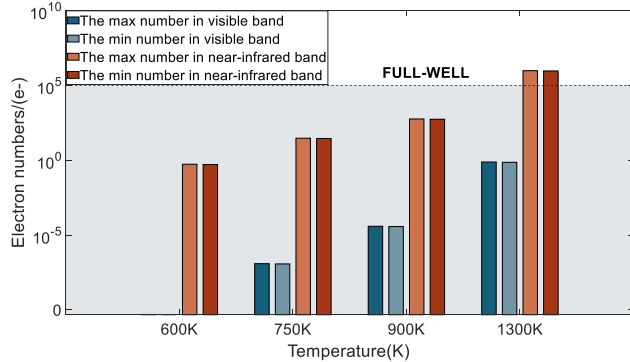window and outer flow is relatively uniform, and an overall suppression method could be used in further study.

FIGURE 5. The maximum and minimum numbers of electrons produced by the high-temperature outer flow on pixels in two bands.

3) FULL-WELL INSPECTION AND SNR CALCULATION

As can be seen in Figs.3-5, in the visible band of 0.35–0.7 μm, the number of electron generated by magnitude 5 stars and noise in pixels did not reach the full-well capacity of a single pixel, even when the observation window temperature was 900 K. When the temperature reached 1300 K, the defocused radiation sources caused all imaging pixels to be full-well. However, in the near-infrared band of 0.9–1.4 μm, when the window temperature reached 750 K, all pixels on the focus plane appeared as full-well.

In the cases in which imaging pixels were not all full-well, the SNR of the brightest and darkest pixels obtained from stars of magnitudes 1–6 could be calculated. This value should be compared with the SNR threshold as $SNR_0 = 3$.

The SNR of the brightest imaging pixel by navigation stars is in the visible band of 0.35–0.7 μm, as shown in Fig.6. Under the influence of 1300 K high-temperature defocused radiation, the SNR values of the brightest pixels of magnitude 1–6 stars were lower than $SNR_0 = 3$. At 900 K, the SNR of the magnitude 5 star's brightest pixel was higher than SNR_0. Under the conditions of 750 K and 600 K, the SNR of the brightest pixels of the magnitude 6 star was higher than 3. This means the brightest pixel could be identified by the sensor.

To identify stars accurately, both the brightest and darkest pixels must be recognized. The SNR of the darkest pixels of stars is shown in Fig.7 for the visible band.

In the visible band of 0.35–0.7 μm, under the influence of 1300 K high-temperature defocused radiation, the darkest pixels' SNR values for all stars were lower than 3. At 900 K, the darkest pixels' SNR values for magnitude 3 stars were higher than 3. When the temperature was further controlled at 750 K and 600 K, the darkest pixels of magnitude 5 stars could be identified. The lower the temperature of the observation window and the outer flow, the higher the SNR of the darkest pixels was in the visible band.

The SNR values of the darkest pixels of stars in the near-infrared band are shown in Fig.8. In the range of 600–1300 K,
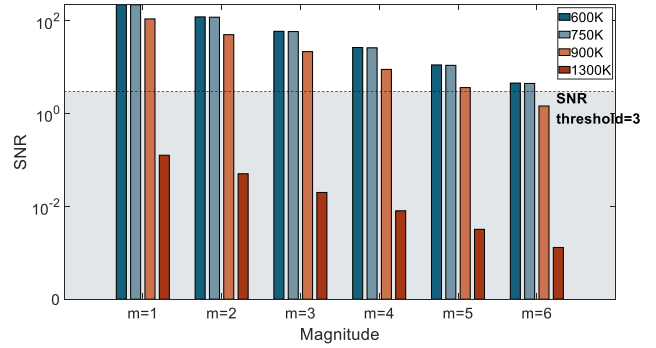

FIGURE 6. The SNR values of the brightest pixels of magnitude 1–6 stars in the visible band.
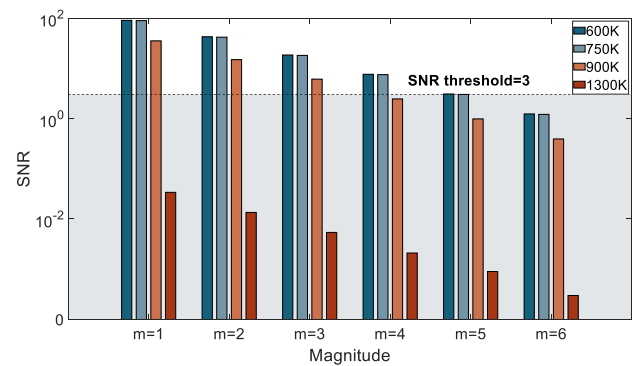

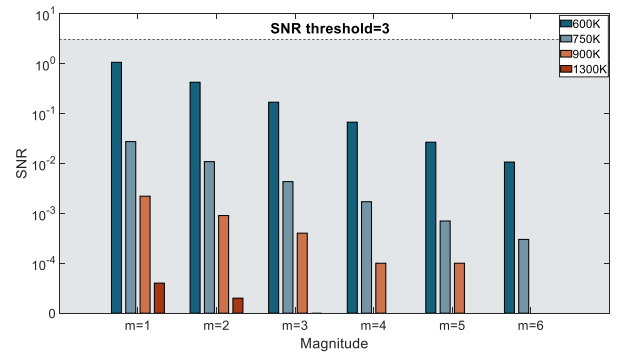**FIGURE 7.** The SNR values of the darkest pixels of magnitude 1–6 stars in the visible band.

FIGURE 8. The SNR of the darkest pixels of magnitude 1–6 stars in the near-infrared band.

it was found that the darkest pixels' SNR for magnitude 1–6 stars did not reach the SNR threshold. This means that the near-infrared band would not be available under a hypersonic thermal environment.

4) LIMITING MAGNITUDE OF OBSERVABLE STARS WITH AEROTHERMAL EFFECT

The previous simulation results showed that the hyperthermal radiation of the observation window under aerodynamic aerothermal conditions was the main source of defocus radiation noise. When the SNR threshold SNR_0 was set as 3,
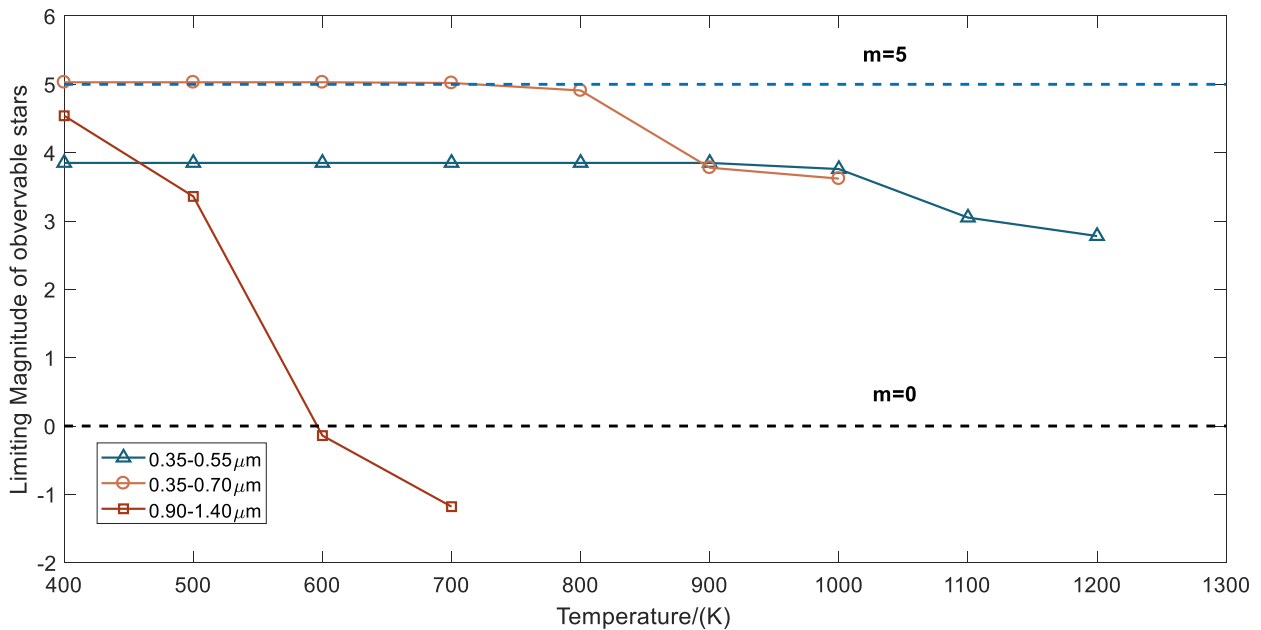
FIGURE 9. The influence of the aerothermal effect on the observable limiting star magnitude.

13 different window temperatures were selected to calculate the observable limiting star magnitude in the bands of 0.35–0.55, 0.35–0.7 and 0.9–1.4 μm. The results are illustrated in Fig. 9. With an increase in the temperature of the observation window and outer flow, the observation capability of the star sensor decreases dramatically. Among those three bands, the observable limiting star magnitude decreased most rapidly in the near-infrared band of 0.9–1.4 μm. The best availability was in the visible band, 0.35–0.7 μm. The curves stop at certain temperatures because stars become unobservable due to saturation of the detector from thermal emission of the optical window.

C. ANALYSIS OF SIMULATION RESULTS

The following conclusions can be drawn from the results of the simulation tests.

(1) The influence of aerothermal effects on astronomical observation under hypersonic flight conditions cannot be ignored. Among these influences, the radiation noise of the hyperthermal observation window itself is significant. Without effective control to keep the temperature of the observation window below 1000 K, the starlight will be completely annihilated in the aerothermal radiation background, making the star sensor unable to effectively capture enough navigation stars.

(2) The observable limiting star magnitude decreases with an increase of the defocused temperature caused by aerothermal heating. In the visible band of 0.35–0.7 μm, when the temperature of the observation window was lower than 750 K, the star sensor with the SNR threshold of 3 could capture navigation stars brighter than magnitude 5. When the temperature was 800 K, it could capture navigation stars brighter than magnitude 4.91. When the temperature reached 900 K,

only stars brighter than magnitude 3.78 could be detected, and finally, above 900 K, it was difficult to capture a stable star map efficiently. Therefore, under certain temperature control conditions, the star sensor in the visible band can detect stars brighter than magnitude 5, thus achieving the basic conditions for astronomical navigation.

(3) The influence of the star sensor working band is significant. The near-infrared band is unavailable under aerothermal conditions. When the temperature was higher than 900 K, the observation performance of the band 0.35–0.55 μm decreased more slowly than that of the visible band. Therefore, to carry out astronomical navigation observation under the influence of aerothermal effects, the band should be properly selected to be far from infrared bands to suppress the influence of high-temperature radiation sources.

(4) The effects of various radiation sources are significantly different. The influence of atmospheric background radiation on imaging is lower than that of the high-temperature outer flow near the window. Furthermore, the influence of the aerothermal flow on imaging is more than two orders of magnitude lower than that of the hyperthermal window. Controlling the temperature of the observation window and suppressing its self-radiation would be the main way to improve the observation ability.

VI. CONCLUSION

This paper constructed the evaluation framework of hypersonic astronomical observation, given the definition of SNR considering defocused radiation sources, and proposed an imaging model of far-field and defocused radiation sources. Full-well inspection, SNR values, and observable limiting star magnitudes were obtained from simulation tests. The relationship between the observable limiting star magnitude

and the window temperature was also determined. It was concluded that star sensors in the visible band should be available on hypersonic vehicles under appropriate temperature control conditions; this finding provides a preliminary basis for performing astronomical window temperature control for future implementations of hypersonic autonomous navigation.

In follow-up work on the application of astronomical navigation technology on hypersonic vehicles, the efficiency of astronomical observation could be improved in the following ways.

(1) The observation capability of stars brighter than magnitude 5 under hypersonic aerothermal influence can be improved by information filtering and fault detection to reduce the initial SNR threshold requirement [29].

(2) Defocused high-temperature radiation noise could be suppressed by improving the image processing capability of star sensors. The noise suppression technology of modern imaging systems has been improved over decades. Uniform noise could be suppressed at the sensor level, based on the results of physical tests and simulations.

(3) The self-radiation of the observation window could be reduced by supersonic film cooling and other technical means [30]. Experiments have shown that the formation of a continuous supersonic film cooling on the surface of the window could control the temperature to remain under 500 K, thus significantly reducing the self-radiation of the window. However, this processing method would form a high-speed tropospheric flow structure on the surface of the window, causing a transition from a laminar flow to turbulence, and posing a separate problem for star map identification.

(4) The degradation of star map may cause measurement faults as special cases of abnormal measurements, which are normally handled by the fault detection technique. The Mahalanobis distance-based technique and robust filtering technique, which handle measurement errors and abnormal measurements and have been used for hypersonic vehicles [31].

REFERENCES

[1] D. Wilkening, "Hypersonic weapons and strategic stability," *Survival*, vol. 61, no. 5, pp. 129–148, Sep. 2019.

[2] B. Chen, Y. Zheng, Z. L. Chen, H. T. Zhang, and X. J. Liu, "A review of celestial navigation system on near space hypersonic vehicle," *Acta Aeronautica Astronautica Sinica.*, vol. 41, no. 8, pp. 32–43, 2020.

[3] Y.-J. Yu, J.-F. Xu, and Z. Xiong, "SINS/CNS nonlinear integrated navigation algorithm for hypersonic vehicle," *Math. Problems Eng.*, vol. 2015, pp. 1–7, Jan. 2015.

[4] J. Lu, C. Lei, and Y. Yang, "A dynamic precision evaluation method for the star sensor in the stellar-inertial navigation system," *Sci. Rep.*, vol. 7, no. 1, pp. 1–12, Dec. 2017.

[5] J. Urzay, "Supersonic combustion in air-breathing propulsion systems for hypersonic flight," *Annu. Rev. Fluid Mech.*, vol. 50, no. 1, pp. 593–627, Jan. 2018.

[6] B. Chen, Y. Zheng, B. Xu, H. T. Zhang, and Z. L. Chen, "Beam deflection correction model of wedge-shaped shock waves over hypersonic vehicles," *Infr. Laser Eng.*, vol. 50, no. 12, 2021, Art. no. 20210182.

[7] V. S. Sudarshanam, M. Cronin-Golomb, P. R. Hemmer, and M. S. Shahriar, "Turbulence-aberration correction with high-speed high-gain optical phase conjugation in sodium vapor," *Opt. Lett.*, vol. 22, no. 15, pp. 1141–1143, 1997.

[8] R. M. Rennie, D. A. Duffin, and E. J. Jumper, "Characterization and aero-optic correction of a forced two-dimensional weakly compressible shear layer," *AIAA J.*, vol. 46, no. 11, pp. 2787–2795, Nov. 2008.

[9] G. Guo and Q. Luo, "Modeling aero-optical wavefront of the forced supersonic mixing layer for adaptive-optic correction," *Opt. Commun.*, vol. 452, pp. 48–55, Dec. 2019.

[10] L. Wu, Q. Xu, H. Wang, H. Lyu, and K. Li, "Guide star selection for the three-FOV daytime star sensor," *Sensors*, vol. 19, no. 6, p. 1457, Mar. 2019.

[11] N. A. Truesdale, K. J. Dinkel, Z. J. B. Dischner, J. H. Diller, and E. F. Young, "DayStar: Modeling and test results of a balloon-borne daytime star tracker," in *Proc. IEEE Aerosp. Conf.*, Mar. 2013, pp. 1–12.

[12] H. Ding, S. Yi, X. Zhao, H. Xiong, and T. Ouyang, "Experimental investigation on aero-optical mitigation of hypersonic optical dome using microvortex generators," *AIAA J.*, vol. 57, no. 6, pp. 2653–2658, Jun. 2019.

[13] D. Wu, Y. Wang, Y. Pu, L. Shang, S. Zhao, and Z. Gao, "Thermal modal test of composite wing structure in high-temperature environments up to 1100°C for hypersonic flight vehicles," *Acta Materiae Compositae Sinica*, vol. 32, no. 2, pp. 323–331, 2015.

[14] G. Guo, Q. Luo, and J. Gong, "Evaluation on aero-optical transmission effects caused by a vortex in the supersonic mixing layer," *Opt. Commun.*, vol. 483, Mar. 2021, Art. no. 126631, doi: 10.1016/j.optcom.2020.126631.

[15] Y. Ni, W. Tan, D. Dai, X. Wang, and S. Qin, "A stellar/inertial integrated navigation method based on the observation of the star centroid prediction error," *Rev. Sci. Instrum.*, vol. 92, no. 3, Mar. 2021, Art. no. 035001.

[16] M. Zhang, Q. Lu, H. Tian, D. Wang, C. Chen, and X. Wang, "Design and optimization for mounting primary mirror with reduced sensitivity to temperature change in an aerial optoelectronic sensor," *Sensors*, vol. 21, no. 23, p. 7993, Nov. 2021.

[17] K. Chen, S.-S. Pei, C.-Z. Zeng, and G. Ding, "SINS/BDS tightly coupled integrated navigation algorithm for hypersonic vehicle," *Sci. Rep.*, vol. 12, no. 1, pp. 1–15, Apr. 2022.

[18] X. Zhao, S. Yi, and H. Ding, "Experimental study on the influence of attitude angle on the aero-optical effects of a hypersonic optical dome," *Optik*, vol. 201, Jan. 2020, Art. no. 163448.

[19] K. K. Zhang, F. Zhou, D. Y. Fu, and T. He, "The study on detect ability calculation method of space object visible camera," *Spacecraft Recovery Remote Sens.*, vol. 27, no. 4, pp. 22–26, 2006.

[20] Y. F. Ma and W. P. Zhao, "Effects of window radiation on infrared imaging detection," *Syst. Eng. Electron.*, vol. 27, no. 32, pp. 427–430, 2005.

[21] Y. M. Cao, W. Zhang, and M. Y. Cong, "Analysis of signal-to-noise ratio calculation for satellite-based infrared staring sensor," *J. Astronaut.*, vol. 28, no. 4, pp. 955–959, 2007.

[22] W. J. Wang, G. J. Zhang, and W. G. Wei, "Modeling analysis and experimental verification for all-time star sensor," *Infr. Laser Eng.*, vol. 48, no. 11, pp. 142–148, 2019.

[23] M. Xu, Q. Feng, and J. Wei, "The calculation of SNR in SWIR detector system for applications to remote sensing," *Infr. Technol.*, vol. 28, no. 10, pp. 588–590, 2006.

[24] L. Q. Han, "Study of the charge transfer mechanism and noise in CMOS active pixels," Ph.D. dissertation, School Electron. Inf. Eng., Tianjin Univ., Tianjin, China, 2016.

[25] Y. H. Li, H. Y. Hu, and Q. Wang, "Radiative transmission property of infrared window in hypersonic vehicle," *Infr. Laser Eng.*, vol. 49, no. 4, pp. 88–94, 2020.

[26] D. Fan, "Thermal optical analysis and design of optical window in high-altitude and high-speed environment," *Infr. Laser Eng.*, vol. 45, no. 8, pp. 1–7, 2016.

[27] F. Xing, *Principle Implement. APS CMOS Star Tracker*, 1st ed. Beijing, China: National Defense Industry Press, 2017.

[28] W. H. Zhang, X. Wang, F. M. Zhang, and G. Q. Ye, "New calculation method for infrared radiation characteristics of nonuniform hot gas," *Infr. Laser Eng.*, vol. 37, no. 4, pp. 573–578, 2008.

[29] G. Gao, B. Gao, S. Gao, G. Hu, and Y. Zhong, "A hypothesis test-constrained robust Kalman filter for INS/GNSS integration with abnormal measurement," *IEEE Trans. Veh. Technol.*, early access, Sep. 23, 2022, doi: 10.1109/TVT.2022.3209091.

[30] S. H. Yi and H. L. Ding, "Research progress of optical aperture with supersonic film cooling under hypersonic flight environment," *Air Space Defense*, vol. 4, no. 4, pp. 1–13, 2021.

[31] B. Gao, W. Li, G. Hu, Y. Zhong, and X. Zhu, "Mahalanobis distance-based fading cubature Kalman filter with augmented mechanism for hypersonic vehicle INS/CNS autonomous integration," *Chin. J. Aeronaut.*, vol. 35, no. 5, pp. 114–128, May 2022.

• • •